Journal of Alloys and Compounds 871 (2021) 159378

Contents lists available at ScienceDirect

Journal of Alloys and Compounds

journal homepage: www.elsevier.com/locate/jalcom

The structural evolution of tetradymite-type Sb_2Te_3 in alkali ion batteries

Conrad Gillard[a], Partha Pratim Jana[b], Maxim Avdeev[c,d], Neeraj Sharma[a,*]

[a] University of New South Wales, Sydney, NSW 2052, Australia
[b] Department of Chemistry, Indian Institute of Technology, Kharagpur, West Bengal 721302, India
[c] Australian Nuclear Science and Technology Organisation, Kirrawee DC, NSW 2232, Australia
[d] School of Chemistry, The University of Sydney, Sydney, NSW 2006, Australia

ARTICLE INFO

Article history:
Received 17 January 2021
Received in revised form 20 February 2021
Accepted 28 February 2021
Available online 3 March 2021

Keywords:
Layered metal chalcogenides
Ex-situ X-ray diffraction
Phase evolution
Alkali ion batteries
Magnetic measurements

ABSTRACT

Tetradymite-type Sb_2Te_3 is synthesised via a solid-state method, and its electrochemical phase evolution in Li, Na and K half-cells is experimentally investigated. Ex-situ X-ray diffraction data is analysed with the Rietveld method, revealing the occurrence of conversion reactions for all systems. Direct evidence of alloying and intercalation reactions is observed in the case of the Li system, while alloying is inferred for the K and Na systems. For the first time, Li intercalated Sb_2Te_3 is synthesised and a preliminary investigation of its magnetic properties is undertaken. Li intercalation does not significantly influence the magnetic phase transition temperature and does not appear to induce superconductivity. In addition, a preliminary study of the performance of Sb_2Te_3 as an electrode material for rechargeable Li, Na and K-half cells is undertaken. High initial capacities of 588, 521 and 906 mAh/g for Li, Na and K cells respectively are observed. However, capacity fade is rapid in all cases, with second discharge capacities dropping to 396, 173 and 98 mAh/g. This poor cyclability is generally associated with the large volume changes and irreversibilities associated with the conversion and alloying reactions. The capacities continue to decrease during extended cycling, with tenth cycle discharge capacities of 195, 26 and 24 mAh/g for Li, Na and K half cells respectively.

1. Introduction

Tetradymite-type Sb_2Te_3 has long been the subject of intense research interest, primarily due to its unusual properties, such as superconductivity [1] and thermoelectric sensitivity [2]. Recently, research interest has been further spurred by the emergence of Sb_2Te_3 as a topological insulator [3] and as a potential phase-change memory device material [4]. The tetradymite-type crystal structure, which has the space group $R\bar{3}m$, consists of a unit cell comprised of 5 monoatomic lamellae with the sequence: Ch-M-Ch-M-Ch, in which Ch denotes a chalcogenide and M a metal. These quintuple layered units are separated by Van der Waals gaps and are stacked along the *c* crystallographic axis [5]. Due to the relatively weak nature of the inter-layer Van der Waals interactions, tetradymite type materials have exhibited the capacity to host intercalating alkali metal ions [6–8] and to permit facile alkali ion diffusion [9–11]. Tetradymite-type materials typically exhibit moderate electrical conductivity, as a consequence of their metallic constituents. For instance, at room temperature the undoped, polycrystalline form of Sb_2Te_3 studied in this work is a semi-conductor, with an electrical resistivity of 2×10^{-1} ohm cm [12].

The electrical conductivity and capability of tetradymites to host intercalants have motivated several studies investigating their potential as alkali ion battery electrode materials [8–11,13–15]. A common finding from these studies was a high first discharge capacity, attributable to the ability of tetradymites to accommodate 12 alkali metal ions per formula M_2Ch_3 unit [8–11,15]. Conversion and alloying reactions were observed, with the general formulae shown in Eqs. 1 and 2 respectively.

$$M_2Ch_3 + 6X \rightarrow 3X_2Ch + 2M \quad (1)$$

$$2M + 6X \rightarrow 2MX_3 \quad (2)$$

In which M denotes a group V metal, Ch denotes a chalcogen and X denotes an alkali metal. A second common finding was poor cycle life, attributable to volume changes associated with the above reactions, although this was improved by nano-engineering or blending techniques [8–11].

The subject of intercalation of alkali ions within tetradymites is of significant interest, as intriguing effects on the electronic properties have been reported. For the case of Bi_2Se_3 the intercalation of 0.12 Cu atoms per formula unit resulted in the emergence of

---

[*] Corresponding author.
E-mail address: neeraj.sharma@unsw.edu.au (N. Sharma).

https://doi.org/10.1016/j.jallcom.2021.159378
0925-8388/

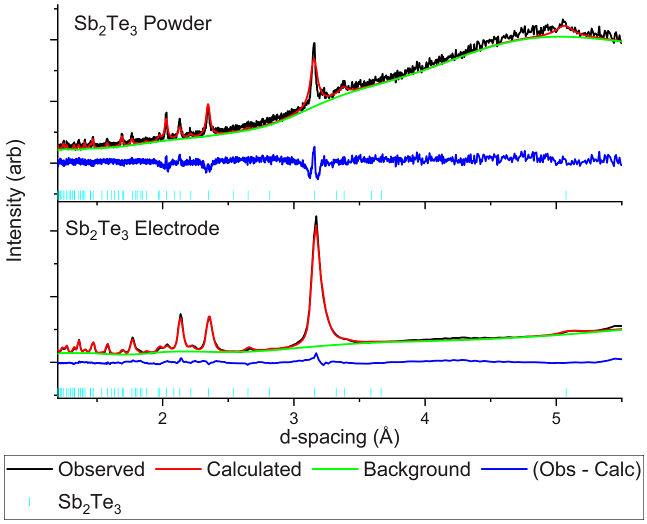

Fig. 1. Rietveld refinement of the Sb_2Te_3 structural model with PXRD data of as-received Sb_2Te_3 powder before and after electrode casting.

Table 1
Rietveld refined model parameters of as-received Sb_2Te_3 powder and processed electrode.

Sample	Sb_2Te_3 *a* (Å)	Sb_2Te_3 *c* (Å)	Zero offset	*wR*
Powder	4.266 (5)	30.45 (1)	0.0220	6.92%
Electrode	4.263 (4)	30.45 (1)	−0.0024	5.52%

superconductivity, with a critical temperature T_c of 3.8 K [16]. Additionally, the electrochemical intercalation of Li in $Bi_2Se_{0.3}Te_{2.7}$ resulted in an improved thermoelectric figure of merit [13]. For the case of Sb_2Te_3, no published studies have examined the effect of intercalation on electronic properties. However electron doping, accomplished by changing the partial pressure of Te during synthesis, resulted in enhanced superconductivity, with a T_c of 8.6 K at ambient pressure, compared to 3 K at 4 GPa for the unmodified form [1,17]. Additionally, the doping of various metals on the lattice sites of Sb_2Te_3 have been found to modify the electronic [18–20] and magnetic properties [21–24]. Specifically, doping of Mn and V induced ferromagnetism [21,23] whereas doping of Fe and Co induced paramagnetism [22,24]. Furthermore, several studies have reported electronic property modification of non-tetradymite type layered metal chalcogenide materials by alkali metal ion intercalation [25–27].

However, conflicting conclusions have been reported regarding electrochemical intercalation within tetradymite-type materials. For the case of Sb_2Te_3 versus Na, Yang et al. [8] reported that an initial downward sloping region of the discharge profile corresponded to an intercalation reaction. Conversely, Nam et al. [9] proposed that the reaction mechanism of this system did not include intercalation. Furthermore, two investigations into the Bi_2Te_3 versus Li system [10,15] did not identify intercalation as a stage of the reaction mechanism. However, in our previous work on Bi_2Te_3 versus Li, the use of ex-situ powder X-ray diffraction (PXRD) produced strong evidence of intercalation within this system [28]. A similar finding was reported by Chen et al., who concluded that intercalation occurred in the $Bi_2Se_{0.3}Te_{2.7}$ versus Li system, also based on ex-situ PXRD data [13]. Contrarily, Ibrahim et al. concluded that intercalation did not occur in the Sb_2Te_3 versus Li system, based on interpretation of the discharge profiles rather than PXRD [11]. These conflicting conclusions may be explicable by methodological differences. Specifically, all studies in which ex-situ PXRD of the electrodes was performed at shallow discharge states concluded that intercalation occurred with these systems as electrodes in Li ion batteries. Whereas those investigations that relied solely on interpretation of discharge curves reached mixed conclusions regarding intercalation. As the collection of ex-situ PXRD data is more conclusive on the crystal structures present, we speculate that these conclusions may be more reliable.

Based on the above analysis, a need to resolve the conflicting claims regarding electrochemical intercalation in the Sb_2Te_3 versus Na system [8,9] and more rigorously investigate the Li system was identified. In this study Sb_2Te_3 was synthesised by a solid-state method and was used to construct lithium, sodium and potassium ion battery electrodes. The cycle life and discharge profiles were measured, and differential capacity plots were calculated. The reaction mechanism was then determined using ex-situ powder X-ray diffraction (PXRD) in conjunction with electrochemical measurements. Additionally, the electrochemical performance and phase evolution of the Sb_2Te_3 versus K system was not previously studied, so this knowledge gap was investigated using a similar method. This study also investigates the magnetic properties of the resultant intercalated materials.

2. Material and methods

Sb_2Te_3 was synthesised via a high temperature solid state method using highly pure Sb (Shot, 6 mm, 99.999% Alfa Aesar) and Te (Powder 99.999% Alfa Aesar). Elements were precisely weighed (approximately 4.5 g each) and loaded inside the glove box and sealed in argon-purged evacuated silica ampoules. The ampoules were heated to 993 K at a rate of 5 K/min and held at this temperature for 96 h. The furnace was then switched off and the samples were allowed to cool to room temperature (RT).

Slurries were prepared by combining ground active material with carbon black powder and polyvinylidene fluoride in a 8: 1: 1 ratio. Sufficient n-methyl-2-pyrrolidone solvent was added to make a thick slurry, and the mixture was stirred in an argon glovebox for 24 h. Following this, the slurry was cast onto a copper foil, using a doctor blade. The resultant electrode sheets were used to construct lithium, sodium and potassium metal half-cells, following standard literature methods [29]. The stainless steel CR2032 coin cell cases, wave springs and spacers were all purchased from MTI. 1 M $LiPF_6$ dissolved in an equivolumetric mixture of ethylene carbonate (EC) and dimethyl carbonate (DMC) and was used as the electrolyte for lithium metal half cells. 1 M $NaPF_6$ and 0.8 M KPF_6 in EC/DMC were used as electrolytes for sodium and potassium metal half cells respectively. After construction, each battery was rested for 24 h then discharged galvanostatically, or in some cases cycled, at a current density of 15 mA/g using a Neware battery cycler. In the case of ex-situ experiments, the batteries were discharged to a targeted state after which they were immediately transferred to an argon filled glovebox and disassembled. The electrodes were removed and washed with dimethyl carbonate in order to remove any electrolyte solution and salts adhered to the surface and left for 24–48 h to allow any residual DMC to evaporate.

Powder X-ray diffraction (PXRD) was used to investigate the structural evolution of the Sb_2Te_3 electrodes. Diffraction patterns were collected using either the Australian Synchrotron or laboratory X-ray diffractometers. For the case of synchrotron experiments, the electrode material was scraped off the current collector, ground using a mortar and pestle, and loaded into a 0.5 mm quartz capillary.

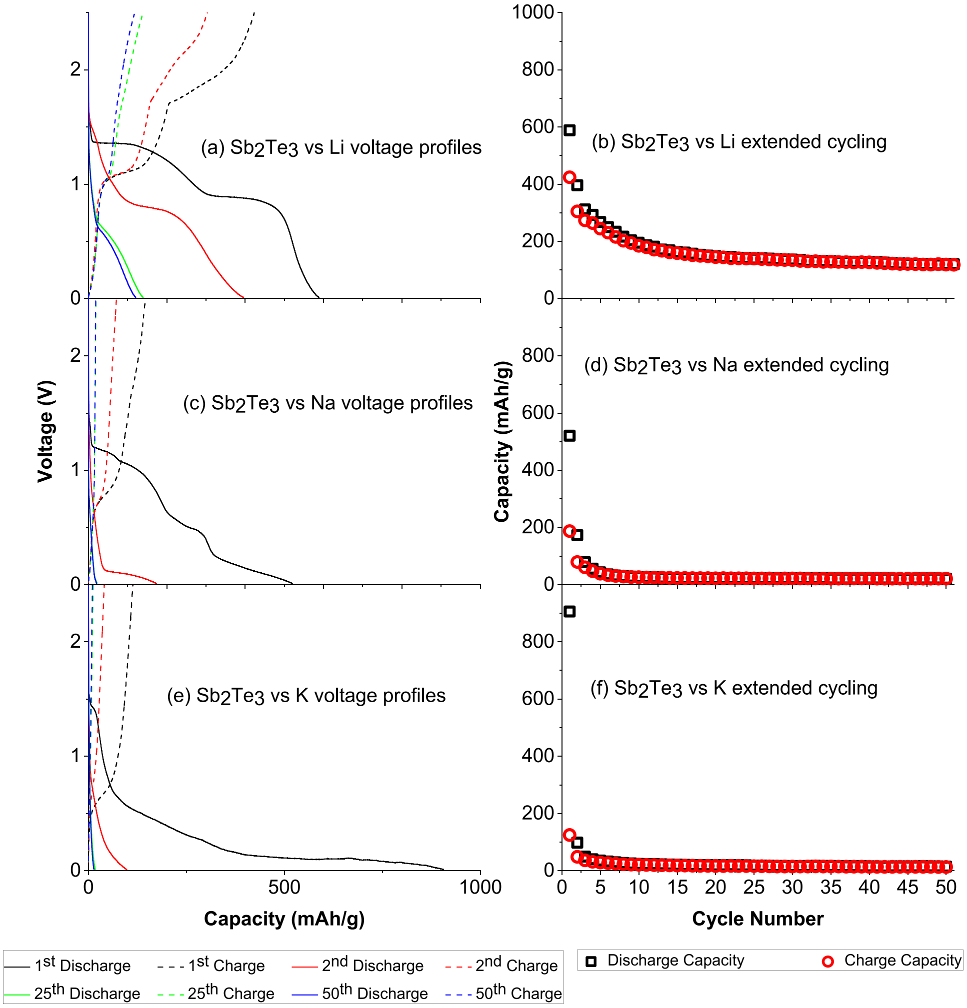

Fig. 2. Selected discharge-charge curves for Sb_2Te_3 versus Li(a) Na(b) and K(c) half cells.

The capillary was sealed with wax before removal from the glovebox. Measurements were performed at the powder diffraction beamline at the Australian Synchrotron, by mounting the capillaries in transmission geometry, utilising a beam size of 3.00 × 1.15 mm and a Mythen microstrip detector [30]. A nominal beam energy of 19 keV was selected and verified by collecting a diffraction pattern from a LaB_6 660b standard and refining the wavelength via the Rietveld method. This resulted in $\lambda = 0.652548(1)$ Å, corresponding to a beam energy of 19.0004(5) keV. For the case of laboratory PXRD experiments, several samples were packed in capillaries and PXRD was performed using either a Stoe Stadi P, or Panalytical Empyrean diffractometer, utilising Mo or Ag Kα radiation respectively. For the majority of samples, the electrode material was scraped off the current collector and transferred to an air-tight sample holder. The sample was not ground, and the sample holder was sealed before removal from the argon filled glovebox. Laboratory PXRD was then performed using a Panalytical MPD diffractometer, utilising Cu Kα radiation. The Rietveld method was used to refine structural models with the PXRD data, using the General Structural Analysis System-II (GSAS-II) software package [31].

DC magnetic susceptibility data was collected from powder samples using a Quantum Design EverCool-II 9 T PPMS with the vibrating sample magnetometry option. Temperature dependent magnetic susceptibility data was collected under zero field cooled (ZFC) and field cooled (FC) conditions upon heating from 3 to 300 K, with an applied field of 1000 Oe.

3. Results and discussion

3.1. Structural evolution during electrode processing

Rietveld refinements of the Sb_2Te_3 structural model using PXRD data collected from an Sb_2Te_3 electrode disc (after processing) and from the as-prepared powder were performed, shown in Fig. 1. The electrode PXRD pattern exhibited peak broadening relative to the powder, however it should be noted that these patterns were collected on different diffractometers. Specifically, the powder was analysed using the Cu source, and the electrode was ground and measured with the Ag source (in a capillary). The broad background feature in the powder sample is attributable to the Kapton foil used to protect the air sensitive sample and is observed in all data collected with Cu source radiation. Lattice parameters and instrument parameters were refined for each sample, and the atomic parameters were left fixed at their initial values. At this stage of the refinement,

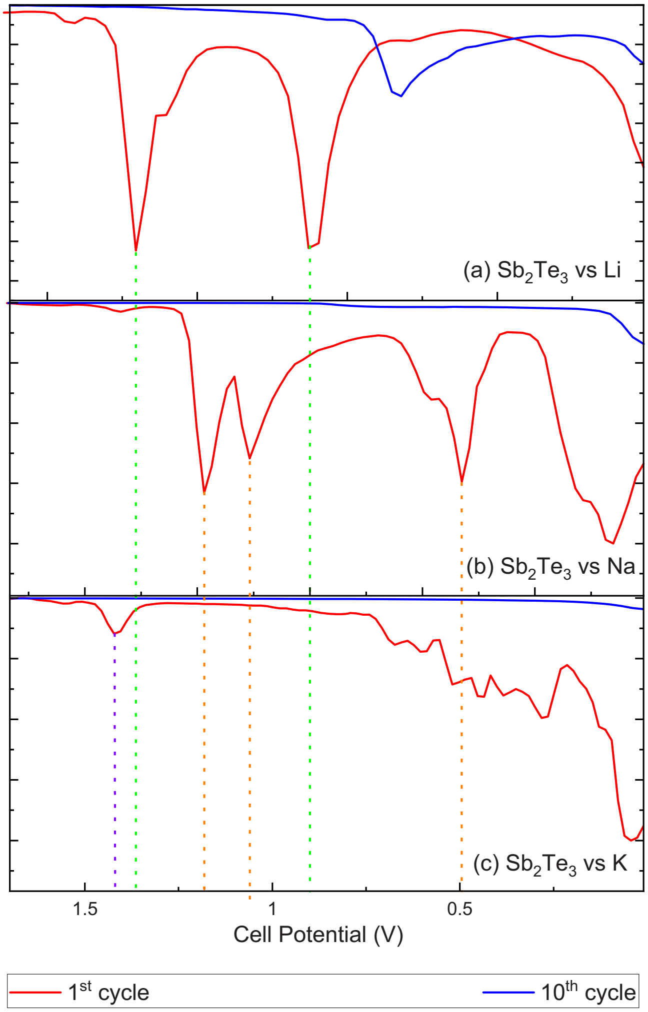

Fig. 3. Differential capacity versus voltage plot for Sb_2Te_3 versus Li(a), Na(b) and K(c) half cells. Droplines indicate the voltages at which features occur.

a mismatch in peak intensities was observed, suggesting a preferred orientation, possibly due to plate-like particle shapes. Consequently the March-Dollase term was refined along the 001 axis, resulting in a close match between measured and calculated peak intensities. A slight mismatch in peak shape was observed for the peak at $d = 3.1$ Å in the powder sample, indicating a minor degree of anisotropic peak broadening. However, attempts to model this via the refinement of uniaxial and generalised strain terms did not produce a significant improvement in visual or statistical fit. Consequently, these parameters were not included in the refinement. We speculate this minor effect may be attributable to the development of a platelet-like morphology. Very minor shifts in certain peak positions were observed, however the *a* and *c* lattice parameters exhibited no statistically significant changes, as shown in Table 1. The similarity of these lattice parameters indicated that minimal structural changes occurred during processing. In order to maintain consistency, the same approach was applied for all refinements based on powdered samples in this work. That is, only the lattice parameters, preferred orientation and instrument parameters were refined.

3.2. Electrochemical performance

Charge-discharge curves and capacity versus cycle number plots for the Li, Na and K half cells are presented in Fig. 2. Large first discharge capacities of 588, 520, 906 mAh/g were exhibited by the Li, Na and K systems respectively. These values were greater than the theoretical capacity of 514 mAh/g, based on the transfer of 12 alkali ions, which is indicative of electrolyte-electrode reactions. All systems displayed rapid capacity fades, with 10th cycle capacity decreases of 67%, 95% and 97% for the Li, Na and K systems respectively. These characteristics were broadly consistent with previous reports on the electrochemical performance of Sb_2Te_3 and other tetradymite-type layered metal chalcogenides [8–11].

The operating voltage of all systems was primarily within the 0–1.5 V window, which suggested a possible application as alkali ion battery anode materials. In order to briefly investigate the commercial viability of this prospect, the performance and price of Sb_2Te_3 was compared to graphite, which is a well-established anode material for lithium ion batteries. Based on prices from Sigma Aldrich for research quantities of these materials, the cost of Sb_2Te_3 exceeded that of battery grade graphite by a factor of 170 [32,33]. In terms of performance, 100th cycle discharge capacities of 250, 200 and 210 mAh/g have been reported for Li, Na and K ion batteries respectively, using graphite or expanded graphite anodes [34–36]. These significantly exceeded the 50th cycle discharge capacities for Sb_2Te_3 reported in this work, which were 110, 21 and 14 mAh/g for Li, Na and K half cells respectively. These comparisons indicate that unmodified Sb_2Te_3 is not an economically competitive alternative for existing alkali-ion battery anode materials. It has been reported that the performance of Sb_2Te_3 in Li and Na ion batteries has been significantly enhanced by nano-engineering [8,9,11]. We speculate that this approach may also improve the performance of Sb_2Te_3 in K ion batteries, and this investigation is suggested for future work.

For the Li system, two clear plateau-like features were observed in the first (and several subsequent) discharge profiles, suggesting that different reactions dominated during these stages of the discharge process. In order to further investigate the electrochemical characteristics, differential capacity plots were formulated, and are presented in Fig. 3. For all systems, a trough at ~0.1 V was observed, corresponding to a sharp drop in potential as full discharge capacity was reached. This was more pronounced in the Na and K systems. The Li system exhibited two distinct features in the form of troughs, corresponding to the end of each plateau region. The Na system likewise exhibited three clear troughs, suggesting that distinct reactions also occurred in this system. In the K system a feature at ~1.5 V was observed, however it was small in magnitude. Inspection of the 10th discharge cycle profile revealed that the Li system preserved the lower potential feature (which shifted in potential) while the other systems did not.

3.3. Sb_2Te_3 versus Li ex-situ experiments

Sb_2Te_3 versus Li half cells were discharged to the states depicted in Fig. 4, and the electrodes were subsequently extracted and analysed with ex-situ PXRD. Compositions are also shown in Fig. 4 and it should be noted that although uncertainties were calculated by Rietveld analyses, error bars are not visible as they are smaller than the data point markers. Rietveld refinements based on structural models with the resultant PXRD data from each sample are shown in Fig. 5, and detailed plots of each refinement are presented in Fig. SI1–6. A table with comprehensive model parameters is also provided in the supplementary information (Table SI1).

The 5% sample exhibited no additional reflections relative to the parent structural model, however Rietveld analysis revealed expansion of the *a* and *c* lattice parameters, as shown in Table 2. This result suggested that the initial downward sloped region of the discharge curve corresponded to the intercalation reaction shown in Eq. 3.

$$xLi + Sb_2Te_3 \rightarrow Li_xSb_2Te_3 \quad (3)$$

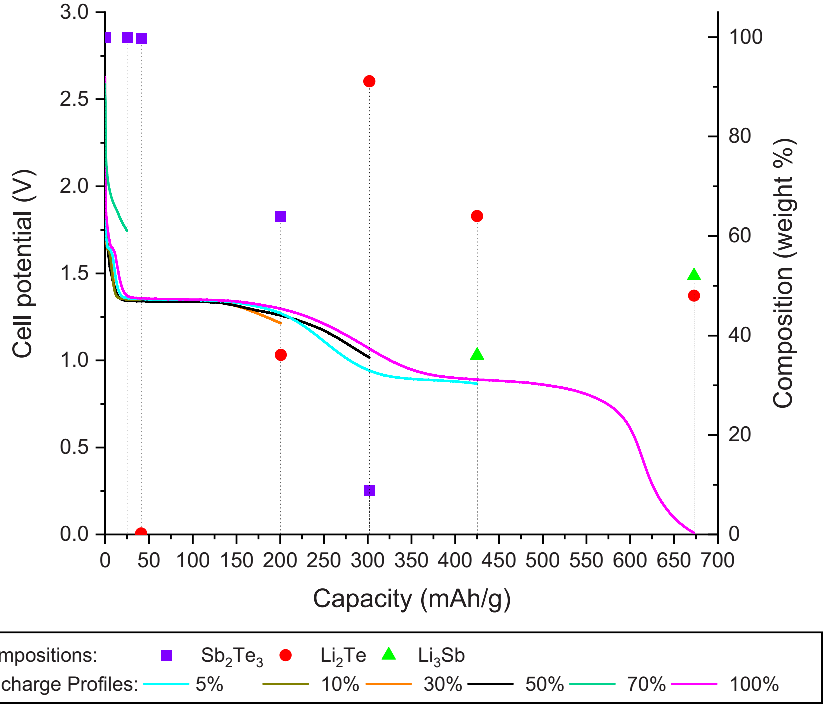

Fig. 4. Discharge profiles and weight fractions of Sb_2Te_3 versus Li ex-situ experiments.

This result contrasts to those published by Nam et al., who did not report the occurrence of intercalation in their experiments on Sb_2Te_3 versus Li half cells [11]. We attribute this difference to our use of Rietveld analysis, which enabled the detection of more subtle aspects of the structural evolution. It should be noted that this was the only Li-discharged sample analysed with the air-sensitive holder rather than a capillary, so it exhibited more pronounced preferred orientation effects.

The 10% discharged sample exhibited several small additional reflections compared to the pristine electrode, for instance at *d*-spacings of 5.1 and 2.7 Å. These reflections were found to be consistent with the formation of Li_2Te. This indicated that following the intercalation reaction proposed above, there was a reaction forming Li_2Te. The reflections attributable to Sb_2Te_3 were slightly shifted, with Rietveld analysis indicating slight expansion of the *a* and *c* lattice parameters.

In the 30% sample the Li_2Te reflections increased in intensity and a further shift in some Sb_2Te_3 peaks was observed. Rietveld analysis showed an increase in the *a* lattice parameter, but no statistically significant change in the *c* lattice parameter. The 50% sample exhibited further expansion of the Sb_2Te_3-type *a* and *c* lattice parameters and increased intensity of the Li_2Te reflections. Taken together, the results of the 10%, 30% and 50% samples suggest that the first pseudo-plateau region corresponded to the simultaneous occurrence of the intercalation reaction shown in Eq. 3, and the conversion reaction shown in Eq. 4.

$$Li_xSb_2Te_3 + (6\text{-}x)Li \rightarrow 3Li_2Te + 2Sb \tag{4}$$

The 70% and 100% samples both showed complete disappearance of the parent peaks, and the presence of a set of reflections slightly offset from those attributed to Li_2Te in the 50% sample. Refinement of the Li_2Te and Li_3Sb structural models resulted in an excellent fit. The 70% and 100% samples were extracted at an intermediate and the end-point of the second plateau-like region of the discharge profile respectively, suggesting that this region corresponded to the alloying reaction shown in Eq. 5.

$$2Sb + 6Li \rightarrow 2Li_3Sb \tag{5}$$

It should be noted that the reflections from the Li_2Te and Li_3Sb phases overlapped, as both phases adopt the same space group and have a similar lattice parameter. Consequently, multiple separate Rietveld analyses were performed, to compare the residuals of fits using only the Li_2Te structural model, or only the Li_3Sb structural model, or both structural models. It was found that although the lattice parameter was only 0.42 Å smaller for Li_2Te than for Li_3Sb, a significantly better fit was accomplished by utilising both structural models.

Additionally, the capacity of the 70% sample was 425 mAh/g, which substantially exceeded the theoretical capacity of 256 mAh/g implied by the conversion reaction shown in Eq. 4. This observed capacity, the diffraction data, and the presence of two plateau-like regions in the discharge profile, are consistent with the occurrence of the above alloying reaction. A similar conclusion was reported by Nam et al. [11]. The discharge capacity of 556 mAh/g observed in the 100% sample slightly exceeds the theoretical capacity of 514 mAh/g, based on the consumption of 12 Li ions per functional unit. The excess capacity is likely due to electrode-electrolyte interactions.

In order to investigate the effect of Li intercalation on the magnetic properties of Sb_2Te_3, magnetometry was performed on the parent material and the 5% discharged sample. Temperature-dependent magnetic susceptibility measurements were collected over a range of 3 – 300 K using Field Cooled Warming and Zero Field Cooled Warming protocols, with an applied magnetic field of 1000 Oe. The room temperature susceptibility of the parent material was -4.2×10^{-7} emu / (g Oe), which was similar though slightly

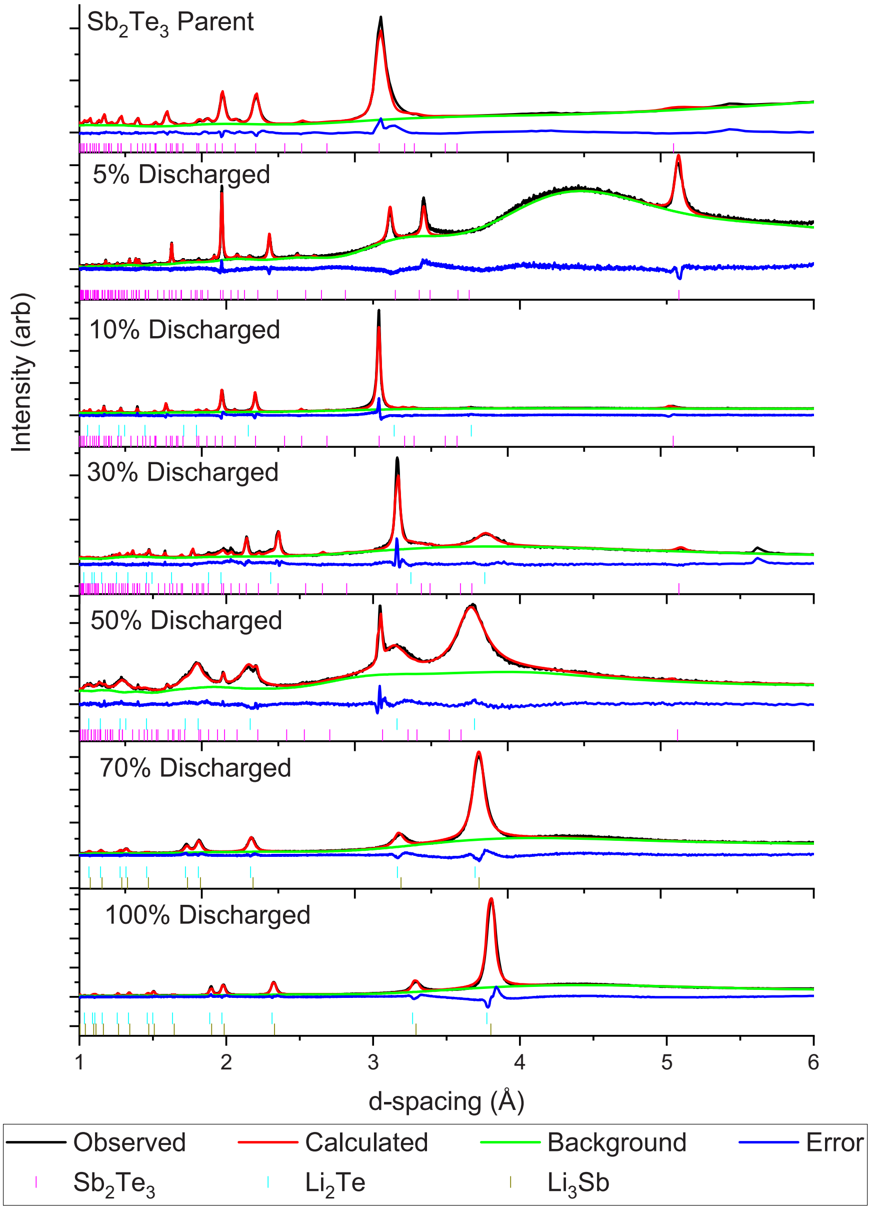

Fig. 5. Rietveld refinements of structural models with PXRD data from Sb_2Te_3 versus Li ex-situ experiments.

Table 2
Lattice parameters and weighted residuals from Rietveld analyses of PXRD data from Sb_2Te_3 versus Li ex-situ experiments.

Sample	Sb_2Te_3 *a* (Å)	Sb_2Te_3 *c* (Å)	Li_2Te *a* (Å)	Li_3Sb *a* (Å)	*wR*
Electrode	4.258 (4)	30.45 (1)			5.92%
5%	4.266 (2)	30.490 (2)			8.46%
10%	4.2672 (4)	30.493 (2)	6.5169 (7)		7.26%
30%	4.271 (2)	30.496 (8)	6.514 (6)		10.22%
50%	4.298 (2)	30.66 (2)	6.553 (2)		4.35%
70%			6.559 (1)	6.604 (4)	7.83%
100%			6.537 (1)	6.584 (2)	9.59%

lower than the typical value of -3.8×10^{-7} emu / (g Oe) reported by Dyck et al. [23]. The parent sample exhibited diamagnetism, which was consistent with reports from the literature [37–42]. It should be noted that although an upward trend at lower temperatures is apparent in Fig. 6, the vertical axis has been magnified in order to highlight the bifurcation between the ZFC and FC curves.

The bifurcation temperatures for the parent and 5% discharged samples were similar, as shown in Fig. 6, suggesting no significant change in magnetic phase transition point. No steep drop in susceptibility was exhibited in the 5% discharged dataset, indicating that superconductivity was not induced. For the 5% sample, the FC profile exhibited a sharp increase in susceptibility with decreasing temperature below the bifurcation point. This suggests that Li intercalation induced paramagnetism, which is consistent with investigations into Sb_2Te_3 doped with Fe and Co [22,24]. However resistivity versus temperature experiments are required to confirm this, and these are recommended for future works.

3.4. *Sb_2Te_3 versus K ex-situ experiments*

Sb_2Te_3 versus K ex-situ PXRD experiments were performed at the discharge states shown in Fig. 7, with the resultant XRD data shown in Fig. 8. A table with comprehensive model parameters is provided in the supplementary information (Table SI2), along with detailed

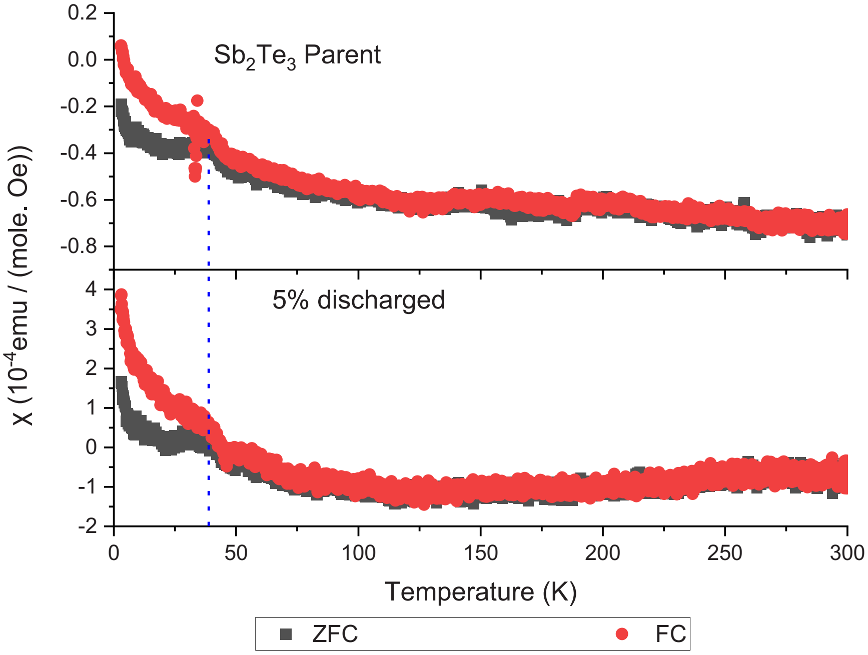

Fig. 6. ZFC and FC curves as a function of temperature for Sb_2Te_3 parent material and Sb_2Te_3 vs Li 5% discharged sample, with an applied field of 1000 Oe.

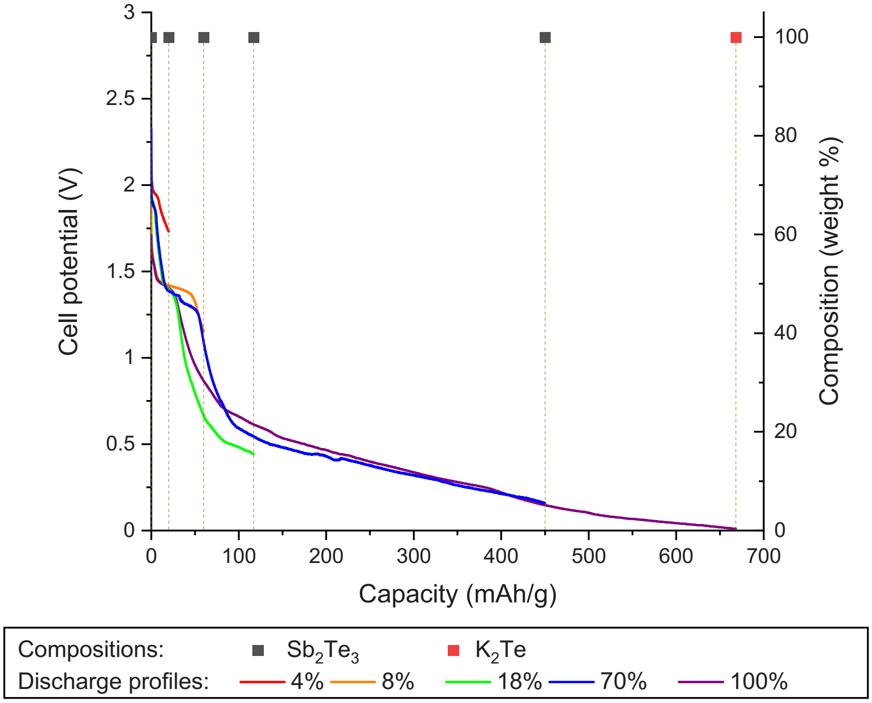

Fig. 7. Discharge profiles and weight fractions for Sb_2Te_3 versus K ex-situ experiments.

plots of each refinement (Figs. SI7–11). The 4%, 8%, 18% and 70% samples exhibited no additional reflections compared to the parent. The *a* lattice parameter expanded very slightly with discharge, with the exception of the 70% sample, which showed a small contraction relative to the 18% sample. The *c* lattice parameter showed no significant change, suggesting that no, or minimal, intercalation occurred for this system. In order to investigate the possibility that intercalation occurred without significant lattice expansion, Fourier

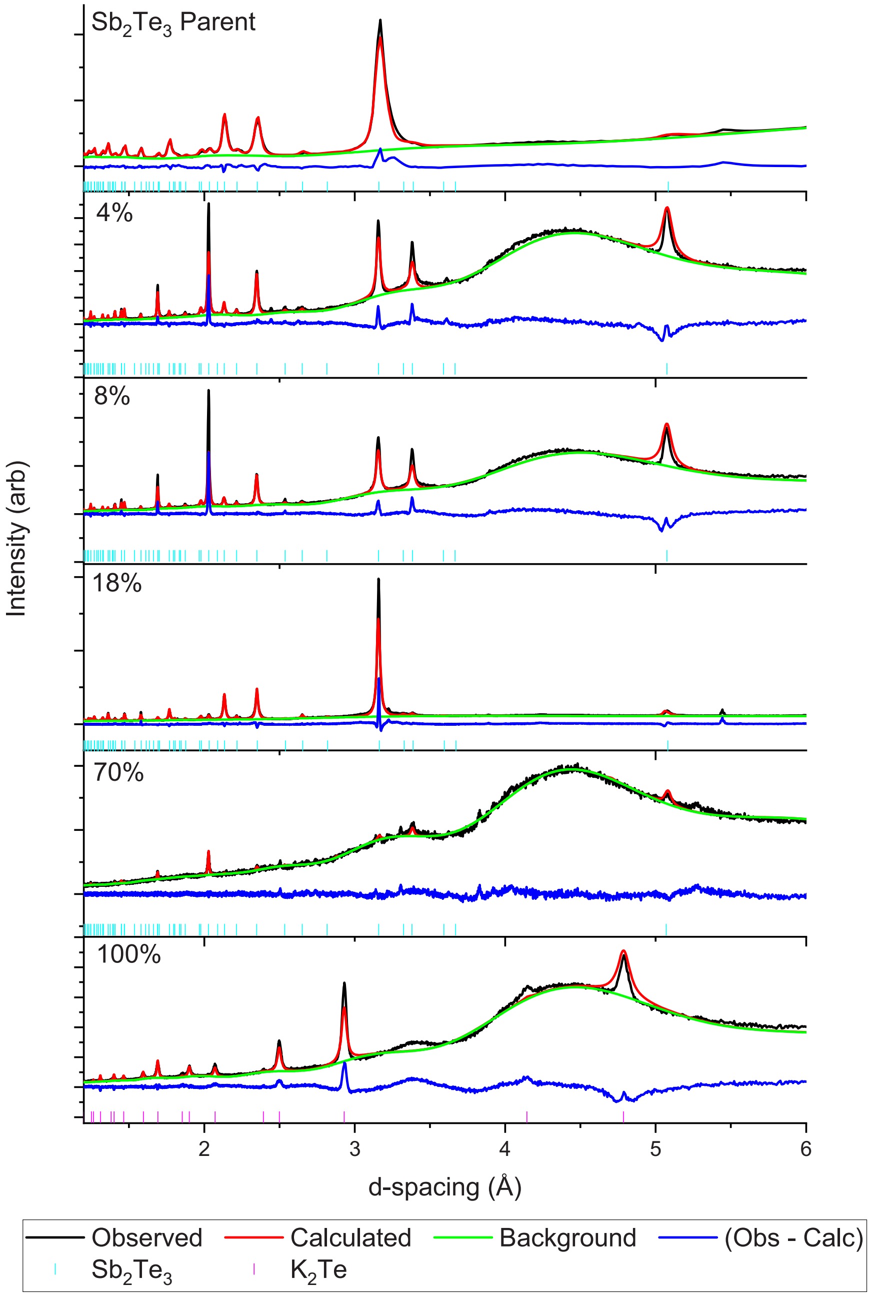

Fig. 8. Rietveld refinements of structural models with PXRD data from Sb_2Te_3 versus K ex-situ experiments.

Table 3
Lattice parameters and weighted residuals from Rietveld analyses of PXRD data from Sb_2Te_3 versus K ex-situ experiments.

Sample	Sb_2Te_3 *a* (Å)	Sb_2Te_3 *c* (Å)	K_2Te *a* (Å)	*wR*
Electrode	4.258 (4)	30.45 (1)		5.92%
4%	4.266 (1)	30.447 (2)		10.68%
8%	4.265 (1)	30.453 (2)		12.78%
18%	4.2687 (3)	30.455 (1)		7.64%
70%	4.263 (4)	30.436 (5)		4.39%
100%			8.289 (1)	8.68%

difference maps were constructed (SI12 – 15). The interlayer gap showed no significant unaccounted electron density, which was consistent with an absence of intercalation (or at least long-range ordered intercalation was insignificant). Interestingly, this contrasted with our previous work on the Bi_2Te_3 versus K system, in which a significant degree of intercalation was observed [28]. This trend is intriguing, given the larger Van der Waals gap of Sb_2Te_3 [28], raising the possibility that ionizability of host materials may be the more significant determinant of intercalation potential in tetradymites. An investigation into whether this trend applies to other tetradymite materials is recommended for future investigations.

The 100% sample exhibited complete disappearance of the parent reflections, and the formation of a new set of reflections that were well matched by the K_2Te structural model. This indicated the occurrence of the conversion reaction shown in Eq. 6.

$$Sb_2Te_3 + 6\,K \rightarrow 3\,K_2Te + 2Sb \tag{6}$$

The capacity of this sample was 668 mAh/g, which substantially exceeded the theoretical capacity of 256 mAh/g implied by the conversion reaction shown in Eq. 6. Based on this capacity, and the observation of an alloying reaction in our previous work on the

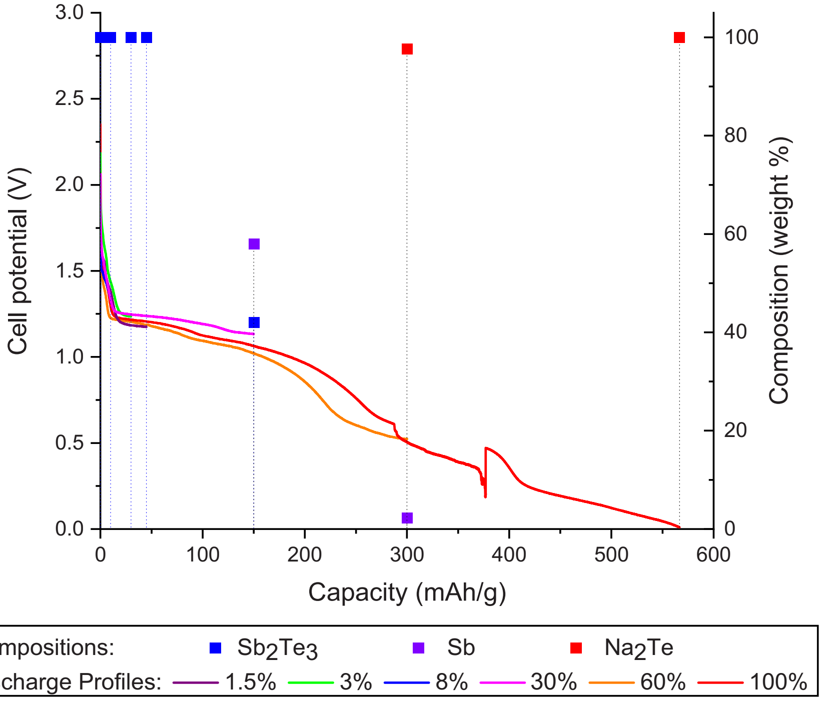

Fig. 9. Discharge profiles and weight fractions for Sb_2Te_3 versus Na ex-situ experiments.

Bi_2Te_3 versus K system [28], we speculate that an analogous alloying reaction occurred in this system, as shown in Eq. 7.

$$2Sb + 6\,K \rightarrow 2\,K_3Sb \tag{7}$$

No reflections consistent with K_3Sb were apparent, and consequently we speculate that a nanosized or nearly amorphous form of this species was generated. The remaining excess capacity observed for the 100% discharged sample is likely attributable to reactions between the electrode and electrolyte. (Table 3).

3.5. Sb_2Te_3 versus Na ex-situ experiments

Sb_2Te_3 versus Na ex-situ PXRD experiments were executed at the states shown in Fig. 9, producing the diffractograms shown in Fig. 10. A table with comprehensive model parameters is provided in the supplementary information (Table SI3), along with detailed plots of each refinement (Figs. SI16–21). The 1.5%, 3% and 8% discharged samples showed no additional reflections relative to the parent, and refinement of the Sb_2Te_3 structural model revealed no statistically significant change in the *c* lattice parameter. A small increase in the *a* lattice parameter was observed in the 1.5% sample, however the 3% and 8% samples showed no change relative to the parent.

The 30% sample exhibited the persistence of the Sb_2Te_3 reflections, and the appearance of a new set of reflections, consistent with the formation of Sb. It should be noted that the Sb reflections were broad, suggesting that a nanosized or nearly amorphous form of this species was generated. Refinement of the Sb_2Te_3 structural model showed no statistically significant change in the *a* and *c* lattice parameters, relative to the parent. The lack of expansion of the lattice parameters suggested that intercalation did not occur in this system. This was further supported by the formulation of Fourier difference maps for the 1.5 – 30% samples (SI22 – 25) which did not exhibit a concentration of unaccounted electron density within the Van der Waals gap. This is contrary to the mechanism proposed by the investigation of Yang et al., in which XRD data was not presented [8]. Our result agrees with that of Nam et al., in which ex-situ XRD data was collected [9]. This is also consistent with our previous work on the Bi_2Te_3 versus Na system, in which intercalation was not observed [28]. The 60% sample exhibited the complete disappearance of the parent reflections, and the appearance of reflections that were well matched by the Sb and Na_2Te structural models. This was indicative of the conversion reaction shown in Eq. 8. As was the case for the 30% sample, the reflections attributable to Sb were broad.

$$Sb_2Te_3 + 6Na \rightarrow 3Na_2Te + 2Sb \tag{8}$$

In the 100% sample, the peaks attributable to Sb had disappeared, and only the set of reflections consistent with Na_2Te remained. Based on the disappearance of Sb, and the large capacity of the cell, we speculate that the alloying reaction shown in Eq. 9 occurred.

$$Sb + 3Na \rightarrow Na_3Sb \tag{9}$$

This hypothesis is further supported by the observation of the same alloying reaction in a similar system. Specifically, an in-situ PXRD study of a Na versus *Pnma*-type Sb_2Se_3 half-cell reported the occurrence of a conversion reaction analogous to Eq. 8, followed by the alloying reaction shown in Eq. 9 at a deeper discharge state. The alloying reaction was evidenced by the appearance of distinct peaks corresponding to Na_3Sb [43] (Table 4).

4. Conclusions

The performance of Sb_2Te_3 as an electrode material for Li, Na and K half cells was measured. High initial discharge capacities of 588, 520 and 906 mAh/g were exhibited by the Li, Na and K systems respectively. However, cyclability was poor, with 10th cycle capacity fades of 67%, 95% and 97% for the Li, Na and K systems respectively. The phase evolution of each system was investigated using ex-situ PXRD in conjunction with the observed discharge profiles. For the case of Li, the reaction mechanism involved a sequence of intercalation, conversion and alloying reactions. However, for the case of

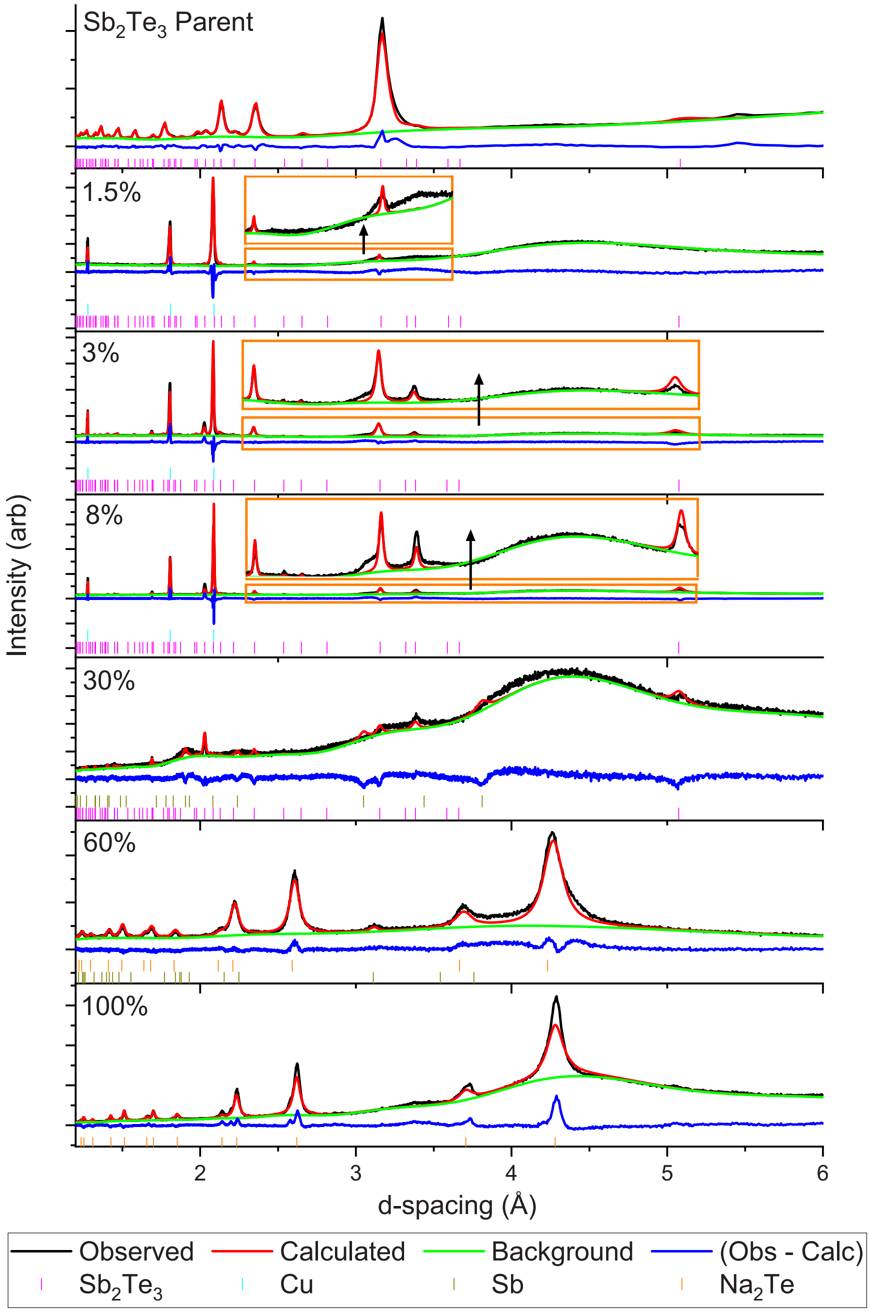

Fig. 10. Rietveld refinements of structural models with PXRD data from Sb_2Te_3 versus Na ex-situ experiments.

Table 4

Lattice parameters and weighted residuals from Rietveld analyses of PXRD data from Sb_2Te_3 versus Na ex-situ experiments.

Sample	Sb_2Te_3 *a* (Å)	Sb_2Te_3 *c* (Å)	Sb *a* (Å)	Sb *c* (Å)	Na_2Te *a* (Å)	*wR*
Electrode	4.258 (4)	30.45 (1)				5.92%
1.5%	4.272 (4)	30.45 (2)				10.07%
3%	4.259 (1)	30.449 (3)				9.47%
8%	4.262 (2)	30.444 (4)				9.99%
30%	4.257 (4)	30.440 (4)	4.162 (5)	11.431 (4)		7.95%
60%			4.30 (2)	11.20 (5)	7.346 (2)	8.247%
100%					7.4149 (1)	10.95%

Na and K, no evidence of intercalation was observed. Several samples exhibited nanosized or near-amorphous species, so future work are proposed to gain insight to these species and the compositional homogeneity of the samples. Techniques such as electron energy loss spectroscopy or total scattering may be suitable for these investigations. The present work constitutes the first reported electrochemical evidence of $Li_xSb_2Te_3$, and a preliminary investigation into the magnetic properties of this material was performed. The bifurcation temperatures of the parent and Li-intercalated materials were similar, suggesting no significant change in magnetic phase transition temperature. The susceptibility versus temperature profiles were suggestive of paramagnetism however resistivity experiments are required to confirm this. Such experiments are recommended for future works.

CRediT authorship contribution statement

Conrad Gillard: Investigation, Data analysis and writing. **Partha Jana:** Methodology, Conceptualisation. **Max Avdeev:** Methodology, Data analysis, Resources. **Neeraj Sharma:** Conceptualisation, Data analysis and writing. All authors contributed to various aspects of the presented research.

Declaration of Competing Interest

The authors declare that they have no known competing financial interests or personal relationships that could have appeared to influence the work reported in this paper.

Acknowledgement

Conrad Gillard was supported by an Australian Government Research Training Program (RTP) Scholarship. Conrad Gillard would also like to thank Australian Institute of Nuclear Science and Engineering (AINSE) Limited for providing financial assistance (Award - PGRA). This work was financially supported by the Australian Research Council Discovery programs (DP200100959 and FT200100707).

Appendix A. Supporting information

Supplementary data associated with this article can be found in the online version at doi:10.1016/j.jallcom.2021.159378.

References

[1] J. Zhu, J.L. Zhang, P.P. Kong, S.J. Zhang, X.H. Yu, J.L. Zhu, Q.Q. Liu, X. Li, R.C. Yu, R. Ahuja, W.G. Yang, G.Y. Shen, H.K. Mao, H.M. Weng, X. Dai, Z. Fang, Y.S. Zhao, C.Q. Jin, Superconductivity in topological insulator Sb_2Te_3 induced by pressure, Sci. Rep. 3 (2013) 2016.

[2] L.W. Da Silva, M. Kaviany, Micro-thermoelectric cooler: interfacial effects on thermal and electrical transport, Int. J. Heat. Mass Transf. 47 (10–11) (2004) 2417–2435.

[3] H. Zhang, C.X. Liu, X.L. Qi, X. Dai, Z. Fang, S.C. Zhang, Topological insulators in Bi_2Se_3, Bi_2Te_3 and Sb_2Te_3 with a single Dirac cone on the surface, Nat. Phys. 5 (6) (2009) 438–442.

[4] B. Liu, Z. Song, S. Feng, B. Chen, Characteristics of chalcogenide nonvolatile memory nano-cell-element based on Sb2Te3 material, Microelectron. Eng. 82 (2) (2005) 168–174.

[5] D.L. Medlin, G. Snyder, Atomic-scale interfacial structure in rock salt and tetradymite chalcogenide thermoelectric materials, JOM 65 (3) (2013) 390–400.

[6] Z. Ding, S.K. Bux, D.J. King, F.L. Chang, T.H. Chen, S.C. Huang, R.B. Kaner, Lithium intercalation and exfoliation of layered bismuth selenide and bismuth telluride, J. Mater. Chem. 19 (17) (2009) 2588–2592.

[7] J. Bludská, I. Jakubec, S. Karamazov, J. Horák, C. Uher, Lithium ions in the van der Waals gap of Bi_2Se_3 single crystals, J. Solid State Chem. 183 (12) (2010) 2813–2817.

[8] Z. Yang, J. Sun, Y. Ni, Z. Zhao, J. Bao, S. Chen, Facile synthesis and in situ transmission electron microscopy investigation of a highly stable Sb2Te3/C nanocomposite for sodium-ion batteries, Energy Storage Mater. 9 (2017) 214–220.

[9] K.-H. Nam, J.-H. Choi, C.-M. Park, Highly reversible Na-ion reaction in nanostructured Sb2Te3-C composites as Na-ion battery anodes, J. Electrochem. Soc. 164 (9) (2017) A2056–A2064.

[10] X.B. Zhao, G.S. Cao, C.P. Lv, L.J. Zhang, S.H. Hu, T.J. Zhu, B.C. Zhou, Electrochemical properties of some Sb or Te based alloys for candidate anode materials of lithium-ion batteries, J. Alloy. Compd. 315 (1–2) (2001) 265–269.

[11] K.-H. Nam, C.-M. Park, Layered Sb_2Te_3 and its nanocomposite: a new and outstanding electrode material for superior rechargeable Li-ion batteries, J. Mater. Chem. A 4 (22) (2016) 8562–8565.

[12] M.M. Ibrahim, M.M. Wakkad, E.K. Shokr, H.A. Abd El-Ghani, Electrical properties of antimony telluride, Appl. Phys. A 52 (4) (1991) 237–241.

[13] J. Chen, X. Zhou, G.J. Snyder, C. Uher, N. Chen, Z. Wen, J. Jin, H. Dong, P. Qiu, Y. Zhou, X. Shi, L. Chen, Direct tuning of electrical properties in nano-structured $Bi_2Se_{0.3}Te_{2.7}$ by reversible electrochemical lithium reactions, Chem. Commun. 47 (44) (2011) 12173–12175.

[14] J. Chen, Z. Sun, Y. Zhu, N. Chen, Y. Zhou, J. Ding, X. Chen, L. Chen, Top-down fabrication of nano-scaled $Bi_2Se_{0.3}Te_{2.7}$ associated by electrochemical Li intercalation, Dalton Trans. 40 (2) (2010) 340–343.

[15] Z. Lijuan, et al., Study on the insertion behaviors of lithium-ions into Bi_2Te_3/polyaniline composites electrodes, Rare Met. Mater. Eng. 4 (2005).

[16] Y.S. Hor, A.J. Williams, J.G. Checkelsky, P. Roushan, J. Seo, Q. Xu, H.W. Zandbergen, A. Yazdani, N.P. Ong, R.J. Cava, Superconductivity in $Cu_xBi_2Se_3$ and its implications for pairing in the undoped topological insulator, Phys. Rev. Lett. 104 (5) (2010) 057001.

[17] L. Zhao, H. Deng, I. Korzhovska, M. Begliarbekov, Z. Chen, E. Andrade, E. Rosenthal, A. Pasupathy, V. Oganesyan, L. Krusin-Elbaum, Emergent surface superconductivity in the topological insulator Sb_2Te_3, Nat. Commun. 6 (1) (2015) 1–8.

[18] P. Lošťák, Č. Drašar, J. Navrátil, L. Beneš, Sb_2Te_3 single crystals doped with chromium atoms, Cryst. Res. Technol. 31 (4) (1996) 403–413.

[19] Č. Drašar, M. Steinhart, P. Lošťák, H.K. Shin, J.S. Dyck, C. Uher, Transport coefficients of titanium-doped Sb_2Te_3 single crystals, J. Solid State Chem. 178 (4) (2005) 1301–1307.

[20] V.A. Kulbachinskii, Z.M. Dashevskii, M. Inoue, M. Sasaki, H. Negishi, W.X. Gao, P. Lostak, J. Horak, A. de Visser, Valence-band changes in $Sb_{2-x}In_xTe_3$ and Sb_2Te_{3-y} Se_y by transport and Shubnikov–de Haas effect measurements, Phys. Rev. B 52 (15) (1995) 10915–10922.

[21] J. Choi, S. Choi, J. Choi, Y. Park, H.M. Park, H.W. Lee, B.C. Woo, S. Cho, Magnetic properties of Mn-doped Bi_2Te_3 and Sb_2Te_3, Phys. Status Solidi B 241 (7) (2004) 1541–1544.

[22] Z. Zhou, M. Žabèík, P. Lošták, C. Uher, Magnetic and transport properties of Sb2−xFexTe3 (0 < x < 0.02) single crystals, J. Appl. Phys. 99 (4) (2006) 043901.

[23] J.S. Dyck, P. Hájek, P. Lošt'ák, C. Uher, Diluted magnetic semiconductors based onSb2−xVxTe3(0.01 < ~x < ~0.03), Phys. Rev. B 65 (11) (2002) 115212.

[24] L. Yang, Z.G. Chen, T. Nie, G. Han, Z. Zhang, M. Hong, K.L. Wang, J. Zou, Co-doped Sb_2Te_3 paramagnetic nanoplates, J. Mater. Chem. C 4 (3) (2016) 521–525.

[25] A.M. Alekseeva, O.A. Drozhzhin, K.A. Dosaev, E.V. Antipov, K.V. Zakharov, O.S. Volkova, D.A. Chareev, A.N. Vasiliev, C. Koz, U. Schwarz, H. Rosner, Y. Grin, New superconductor $Li_xFe_{1+\delta}$ Se (x≤ 0.07, T c up to 44 K) by an electrochemical route, Sci. Rep. 6 (2016) 25624.

[26] T. Kajita, T. Kawamata, T. Noji, T. Hatakeda, M. Kato, Y. Koike, T. Itoh, Electrochemical Na-intercalation-induced high-temperature superconductivity in FeSe, Phys. C Supercond. Appl. 519 (2015) 104–107.

[27] Y. Takahei, K. Tomita, Y. Itoh, K. Ashida, J.H. Lee, N. Nishimoto, T. Kimura, K. Kudo, M. Nohara, Y. Kubozono, T. Kambe, A new way to synthesize superconducting metal-intercalated C_{60} and FeSe, Sci. Rep. 6 (2016) 18931.

[28] C.H. Gillard, et al., Electrochemical phase evolution of tetradymite-type Bi_2Te_3 in lithium, sodium and potassium ion half cells, J. Alloy. Compd. (2020) 155621.

[29] T. Marks, S. Trussler, A.J. Smith, D. Xiong, J.R. Dahn, A guide to Li-ion coin-cell electrode maFking for academic researchers, J. Electrochem. Soc. 158 (1) (2011) A51–A57.

[30] Wallwork, K.S. , B.J. Kennedy , and D. Wang . The high resolution powder diffraction beamline for the Australian Synchrotron. in AIP Conference Proceedings. 2007. AIP.

[31] B.H. Toby, R.B. Von, Dreele, GSAS-II: the genesis of a modern open-source all purpose crystallography software package, J. Appl. Crystallogr. 46 (2) (2013) 544–549.

[32] Sigma-Aldrich. Antimony(III) *telluride* [cited 21 August 2020]; https://www.sigmaaldrich.com/catalog/product/aldrich/733490?lang=en&region=AU.

[33] Sigma-Aldrich. Graphite anode powder [cited 19 April 2020]; https://www.sigmaaldrich.com/catalog/product/aldrich/907154?lang=en&region=AU.

[34] Y. Wen, K. He, Y. Zhu, F. Han, Y. Xu, I. Matsuda, Y. Ishii, J. Cumings, C. Wang, Expanded graphite as superior anode for sodium-ion batteries, Nat. Commun. 5 (1) (2014) 1–10.

[35] L. Fan, R. Ma, Q. Zhang, X. Jia, B. Lu, Graphite anode for a potassium-ion battery with unprecedented performance, Angew. Chem. Int. Ed. 58 (31) (2019) 10500–10505.

[36] Y.-P. Wu, E. Rahm, R. Holze, Carbon anode materials for lithium ion batteries, J. Power Sources 114 (2) (2003) 228–236.

[37] B. Roy, B.R. Chakraborty, R. Bhattacharya, A.K. Dutta, Electrical and magnetic properties of antimony telluride, Solid State Commun. 25 (8) (1978) 617–620.

[38] Kabir, F. et al., Effect of dilute magnetism in a topological insulator. arXiv preprint arXiv:2006.14130, 2020.

[39] J. Horák, M. Matyáš, L. Tichý, Lattice defects in manganese-doped Sb_2Te_3 crystals, Phys. Status Solidi A 27 (2) (1975) 621–626.

[40] A. Van Itterbeek, N. Van Deynse, C. Herinckx, Measurements on the magnetic anisotropy of single crystals of Bi2Te3, Sb2Te3 and compounds of them, between room temperature and 1.3° K, Physica (1966) 2123–2128.

[41] M. Abou-Sekkina, Further investigations on the temperature-dependence of magnetic susceptibility and thermogravimetry of stoichiometric antimony triselenide and antimony tritelluride semiconductors, J. Therm. Anal. 34 (1) (1988) 155–159.

[42] N.P. Stepanov, A.K. Gil'fanov, L.D. Ivanova, Y.V. Granatkina, Magnetic susceptibility of Bi_2Te_3-Sb_2Te_3 alloys, Semiconductors 42 (4) (2008) 401–405.

[43] X. Ou, C. Yang, X. Xiong, F. Zheng, Q. Pan, C. Jin, M. Liu, K. Huang, A new rGO-overcoated Sb_2Se_3 nanorods anode for Na+ battery: in Situ X-ray diffraction study on a live sodiation/desodiation process, Adv. Funct. Mater. 27 (13) (2017) 1606242.